PNAS

Supplementary Information for

White Matter Plasticity Following Cataract Surgery in Congenitally Blind Patients

Authors: Caterina A. Pedersini [a,1], Nathaniel P. Miller [b,1], Tapan Gandhi [c,1], Sharon Gilad-Gutnick[d], Vidur Mahajan[e], Pawan Sinha[d], Bas Rokers [a,f,2]

Affiliations:
[a] Psychology, Division of Science, New York University Abu Dhabi, United Arab Emirates
[b] University of Minnesota Medical School – Minneapolis, MN 55455, United States of America
[c] Department of Electrical Engineering, Indian Institute of Technology, New Delhi, Delhi 110016, India
[d] Department of Brain and Cognitive Sciences, Massachusetts Institute of Technology, Cambridge, MA 02139, United States of America
[e] Mahajan Imaging Center, Defence Colony, New Delhi, Delhi 110016, India
[f] ASPIRE Precision Medicine Research Institute, Abu Dhabi, United Arab Emirates

[1] Contributed equally

[2] Corresponding Author: rokers@nyu.edu

This PDF file includes:
SI Method
SI Results
Tables S1 to S5
Figures S1 to S5
SI References

SI Method

Pre-Processing

For the sample of patients, as data were collected only in one phase-encoded direction ("AP" in the majority of cases), we applied a deep learning approach (named Synb0-DisCo) after denoising and removing Gibbs Ringing Artifacts, to estimate the spatial distortions due to susceptibility- induced off-resonance fields (2, 3). This tool synthesizes an "undistorted" b=0 image to be used in standard pipelines, such as FSL's TOPUP algorithm, which traditionally requires data acquired with two opposite phase encoding directions (4, 5).Thus, after performing image synthesis, FSL's TOPUP algorithm and removing non-brain tissue from the resulting undistorted and synthetized b=0 data, we applied eddy correction with outlier replacement as implemented in the FMRIB Software Library (FSL), to correct for eddy current and subject movements. The corrected images were finally co-registered to the AC-PC-aligned T1-weighted image and diffusion tensors were fitted to the volume using a least-squares estimate bootstrapped 500 times (6).

Aside from the initial off-resonance field compensation step, pre-processing steps were completed using the VistaSoft software package (Stanford University, Stanford, California). Processing was done independently for each participant.

Data from the sample of controls were preprocessed by running the HCP Structural and Diffusion Preprocessing Pipelines, as part of the HCP Minimal Preprocessing pipeline (7).

ROI Placement

For both patients and controls, we used an automated method to identify regions of interest (ROIs) along the brain's early visual pathway. Optic Chiasm (OC) and Primary Visual Cortex (V1) ROIs were generated automatically in native T1-weighted anatomical space using FreeSurfer (8). To segment the thalamus we used an additional tool of Freesurfer that generates a probabilistic atlas of the human thalamic nuclei for each participant, in the native T1-weighted anatomical space (9). In this way we extracted the Lateral Geniculate Nucleus (LGN) ROIs that allowed us to track the Optic Radiation. All the ROIs were coregistered to AC-PC space and downsampled to the diffusion resolution.

Visual System Tractography

The optic tract and optic radiation white matter pathways were derived through probabilistic tractography using MRtrix3 in both patients and controls (Brain Institute, Melbourne, Australia) (10–19). First, we extracted a five-tissue-type segmented image from the T1-weighted data coregistered to AC-PC space. Then, we estimated response functions (20) and fiber orientation distribution (FOD) (21) using constrained spherical deconvolution (CSD) to generate fibers between left and right optic tract ROI pairs (OC » LGN) and left and right optic radiation ROI pairs (LGN » V1) by applying a Second-order Integration algorithm over Fiber Orientation Distributions (22).

The maximum number of streamlines was set to 10,000. Final pathways were restricted to fibers passing between the specified ROIs, omitting any spurious results. This automatic fiber cleaning was performed by removing all fibers that terminate in the Thalamus but outside the ROIs. No additional manual cleaning was performed.

In addition, a whole-brain tractography was completed using a maximum of 5,000,000 fibers. For all analyses, diffusion measures from the left and right optic tract and optic radiation pathways were averaged across hemispheres. An illustration of these visual pathways in a representative patient (P02) is shown in Fig. 2A (left column).

Cortical Pathway Tractography

A total of 20 cortico-cortical whole-brain pathways were generated using the Automated Fiber Quantification toolkit (23–25). Whole-brain streamlines tracking (STT) tractography was performed for all subjects, with 20 major pathways isolated, constrained, and cleaned automatically. A total of eight combined pathways were included in the analysis: the callosum forceps major (or posterior callosum forceps), inferior fronto-occipital fasciculus (IFOF), inferior longitudinal fasciculus (ILF), superior longitudinal fasciculus (SLF), corticospinal tract (CST), cingulum cingulate (CC), callosum forceps minor (or anterior forceps) and the uncinate fasciculus (UF). For all analyses, the left and right IFOF, ILF, SLF, CST, CC and UF pathways were averaged between hemispheres. A render of these pathways in a representative patient is provided in Fig. 2A (central and right column).

Diffusion Measures

Diffusion properties were sampled from all voxels within the volumetric region defined by each white matter pathway. The diffusion properties included in our analyses were mean diffusivity (MD, $\mu m^2/s$) and fractional anisotropy (FA). MD is a measure of average diffusivity partially related to myelination (26), where immature developing pathways have higher measures of MD, with decreasing values over the developmental time course. FA provides a more complex measure of diffusion directionality and is highly sensitive to microstructural changes in a variety of pathologies. In the typical developmental trajectory, FA increases over time as pathways mature. Different pathways follow different developmental trajectories and vary in their average MD and FA values over time, but generally follow trends of decreasing MD and increasing FA with white matter maturation through middle to late adulthood (27–30).

Analysis

Individual white matter pathways were isolated from the MRI data collected during each subject's longitudinal scan and diffusion properties were sampled from the volumetric region defined by these pathways in the corresponding longitudinal dMRI data point.

To assess diffusion properties and normalize pathway lengths across subjects, 100 evenly-spaced samples were taken along the length of each pathway. Thus, 100 averaged MD and FA values were sampled from 10 white matter pathways for every longitudinal dMRI time point for all cataract patients. These cross-sectional samples were generated from a gaussian-weighted average, where diffusion measures extracted from tensors in the central "core" of each pathway were selectively weighted over tensors in outlying fibers. Of these 100 samples, only the middle 80 were analyzed to reduce the risk of including aberrant diffusion measures occurring at the interface of gray- and white matter or in regions of crossing fibers (as in the optic chiasm) (1, 31). These middle 80 samples were averaged, so a single mean MD/FA value was available for each pathway at each longitudinal time point for all cataract patients.

Linear mixed effects (LME) models were used to evaluate the longitudinal effects of maturation and cataract surgery on white matter development in patients. The first family of LME models included only patient and were formatted as follows:

*Pathway MD/FA ~ Log DaysSinceSurgery * Age at Measurement + (1 | Subject)*

In this case, each model included fixed effects of the age at diffusion measurement, the logarithm (log10) of the time since surgery (days since surgery; DSS), an interaction between age and DSS and the random effect of subjects. In the other sections of the paper, we will refer to this family of LME models as patients-only analysis.

In order to be able to assess the typical development of diffusion measures in healthy controls and to discern between maturational and surgery changes in patients, we included a second family of LME models on the complete sample, adding the fixed-effect of Group:

*Pathway MD/FA ~ Group + Log DaysSinceSurgery * Age at Measurement + (1 | Subject)*

In the other sections of the paper, we will refer to this family of LME models as controls-included analysis.

For each family, a total of 20 LME models were evaluated, predicting MD and FA values for each of the 10 included pathways. From each model we extracted the Variational Inflation Factor (VIF) to avoid the presence of collinearity between predictors. Moreover, we performed a cross-validation of the LME by performing a leave-one-out to predict the diffusion measure of one session based on all the other timepoints. Significant correlation coefficients would indicate that the model can correctly predict the empirical dependent variable.

When including controls to the model, arose the problem of assigning values to the logarithmic scale of the time since surgery of controls. In order to assess the stability of the results, we assigned different values to this variable, going from a constant value (=log10(1) or the mean of log time since surgery of patients), to a random assignation of values belonging to a range from 0 to the logarithmic scale of age at measurement of controls. To do that, we repeated each LME 5000 times while assigning random values to time since surgery of controls. This sequence of iterations allows us to plot the distribution of p-values per tract (20), structural measure (2) and effect (time since surgery and interaction effect). The percentage of significant p-values will give a descriptive measure of how independent the results are from the specific value assigned to the controls.

In the main manuscript we describe the results obtained by assigning the mean values of patients to controls, based on the lowest VIF and on the assumption that the structural measures extracted from controls should be more similar to the structural measures extracted from patients at a certain time after surgery than at the day of surgery. In addition, we provide a complete description of the results in the supplementary material, to show the stability of our findings.

Finally, in the attempt to reduce the differences in sequence acquisition between samples that could lead to a statistical difference in the structural measures, we performed the analysis either on all diffusion volumes of controls (199) and on a subsample of diffusion volumes with a b-value close to the one used in the sequence of patients (b<1500). In the main manuscript we describe the results obtained by including only the subsample of diffusion volumes with a b-value < 1500 because of a higher similarity with the sequence used for patients. We still provide the final results of the LME using all volumes of controls in Table S3 and S4.

Before running the LME models, we removed the outliers separately for each group, for each measure and tract by applying the Median Absolute Deviation (MAD) method. As a result, we included a different number of points in the final analysis for different tracts. To correct for multiple-comparisons, the Benjamini and Hochberg False Discovery Rate (FDR) test was used (32) separately for FA and MD values. To do that, we pooled the P-values from ANOVAs of the fixed and interaction effects for each dMRI measure (FA and MD) and each tract (20) and calculated the corresponding FDR values. Thus, we obtained a total amount of 60 FDR values, 30 for each dMRI measure (FA or MD). P-values from ANOVAs of the fixed and interaction effects for all 20 LME models were pooled and an FDR value was calculated for each (30 FDR values for FA and MD). Effects with an FDR value smaller than our target alpha ($\alpha < 0.05$) were regarded statistically significant. For each tract we reported the F-statistic as well as the p-value before and after FDR correction for each fixed main effect and interaction. In Fig. S4 we reported R^2 values adjusted for the number of predictor variables in the model.

To assess the association between surgery, structural measures changes and behavioral outcome, we performed a mediation analysis using the MATLAB-based mediation toolbox described by Wager et al. (2008) (33) available at: https://github.com/canlab/MediationToolbox.

The test is based on three criteria: 1). The initial variable (surgery) must be related to the mediator (structural measure) and this relation defines the path a; 2). The mediator must be related to the outcome (performance) after controlling for the initial variable and this relation defines the path b; 3). The mediation effect must be significant. This is defined as product of the a (initial variable-mediation) and b (mediator-outcome) path coefficients (a*b). A significant mediation effect indicates that the mediator significantly reduces the predictor-outcome relationship as their association is transmitted through a mediator. In this study, we tested the mediation effect either with and without controlling for the moderation effect, by adding or

removing the interaction between initial variable and mediator to the regression model. This was done to assess whether the structural measure was referable as a mediator, a variable through which the initial variable is transmitting its influence on the outcome, or as a moderator, a variable that affects the outcome by interacting with the initial variable.

SI Results

In the manuscript we explored different LME models and assigned multiple values to time since surgery in controls. In the following tables we are showing the results according to the different models or values used, starting from the patient-only model results (table S1).

A — *Fractional Anisotropy*

	Pathway	Age	Time Since Surgery	Age * Time Since Surgery
Early Visual	*Optic Tract*	0.055	**0.023**	**0.008**
	Optic Radiation	0.142	0.078	0.052
Late Visual	*Callosum Forcepts Major*	**0.013**	0.108	0.059
	Inferior Fronto-Occipital Fasciculos	0.116	**0.012**	**0.034**
	Inferior Longitudinal Fasciculus	**0.002**	**0.011**	**0.004**
	Superior Longitudinal Fasciculus	**0.016**	**0.012**	**0.009**
Motor	*CorticoSpinal Tract*	0.666	0.366	0.476
Other	*Cingulum Cingulate*	0.123	0.257	0.264
	Callosum Forcepts Minor	0.286	**0.041**	0.133
	Uncinate Fasciculus	0.105	0.058	0.078

B — *Mean Diffusivity*

	Pathway	Age	Time Since Surgery	Age * Time Since Surgery
Early Visual	*Optic Tract*	**0.021**	0.093	0.116
	Optic Radiation	0.143	0.311	0.457
Late Visual	*Callosum Forcepts Major*	0.368	**0.000**	**0.001**
	Inferior Fronto-Occipital Fasciculos	0.298	0.613	0.359
	Inferior Longitudinal Fasciculus	0.130	0.955	0.681
	Superior Longitudinal Fasciculus	**0.043**	0.135	0.390
Motor	*CorticoSpinal Tract*	0.012	0.224	0.302
Other	*Cingulum Cingulate*	**0.034**	0.928	0.643
	Callosum Forcepts Minor	0.089	**0.041**	0.215
	Uncinate Fasciculus	0.095	0.464	0.936

Table S1. Summary of fractional anisotropy and mean diffusivity changes in early-, late- and non-visual pathways in patients-only analysis. P-values for main effects of age, time since surgery (log10), and age * time since surgery (log10) interaction for ten visual and non-visual pathways. P-values smaller than 0.05 are colored light blue while bold values indicate significant effects after false-discovery rate (FDR) correction at $\alpha = 0.05$.

The controls-included analysis was performed by assigning different values to the time since surgery of controls. Results described in the main manuscript refer to the assignment of the mean value of patients for all controls, but we performed the analysis also assigning 0, simulating that structural measures of controls would have been similar to structural measures of patients at the day of surgery. Table S2 shows the results assigning 0 to all controls.

A — *Fractional Anisotropy*

	Pathway	Group	Age	Time Since Surgery	Age * Time Since Surgery
Early Visual	*Optic Tract*	0.112	0.810	0.134	0.068
	Optic Radiation	0.084	**0.002**	0.081	**0.039**
Late Visual	*Callosum Forcepts Major*	0.412	**0.019**	0.365	0.284
	Inferior Fronto-Occipital Fasciculos	0.241	**0.000**	**0.006**	**0.010**
	Inferior Longitudinal Fasciculus	0.834	**0.000**	**0.027**	**0.013**
	Superior Longitudinal Fasciculus	0.835	**0.000**	**0.020**	**0.011**
Motor	*CorticoSpinal Tract*	**0.000**	0.176	0.073	0.062
Other	*Cingulum Cingulate*	0.587	**0.000**	0.169	0.129
	Callosum Forcepts Minor	**0.011**	0.661	0.062	0.241
	Uncinate Fasciculus	0.542	0.223	0.122	0.199

B — *Mean Diffusivity*

	Pathway	Group	Age	Time Since Surgery	Age * Time Since Surgery
Early Visual	*Optic Tract*	**0.000**	0.148	0.551	0.934
	Optic Radiation	**0.000**	**0.000**	0.789	0.958
Late Visual	*Callosum Forcepts Major*	**0.000**	**0.003**	**0.000**	**0.000**
	Inferior Fronto-Occipital Fasciculos	**0.000**	**0.000**	0.805	0.456
	Inferior Longitudinal Fasciculus	**0.000**	**0.000**	0.748	0.972
	Superior Longitudinal Fasciculus	**0.000**	**0.000**	0.056	0.197
Motor	*CorticoSpinal Tract*	**0.000**	**0.000**	0.109	0.116
Other	*Cingulum Cingulate*	**0.000**	**0.000**	0.944	0.574
	Callosum Forcepts Minor	**0.000**	**0.003**	**0.017**	0.248
	Uncinate Fasciculus	**0.000**	**0.000**	0.338	0.893

Table S2. Summary of fractional anisotropy and mean diffusivity changes in early-, late- and non-visual pathways in controls-included analysis. P-values for main effects of group, age, time since surgery (log10), and age * time since surgery (log10) interaction for ten visual and non-visual pathways when assigning 0 to the time since surgery of controls. P-values smaller than 0.05 are colored light blue while bold values indicate significant effects after false-discovery rate (FDR) correction at $\alpha = 0.05$.

P-values of the main fixed- and interaction-effect of the LME are shown in table S3 (FA) and S4 (MD). In A) we describe the results using a reduced number of volumes, to control for differences in the acquisition sequence between patients (B=1000) and controls (multishell acquisition). In B) we describe the results using all volumes of controls. These results are less reliable as the differences in the acquisition protocol can be the source of the significant

differences observed between groups in almost all tracts. An example of a plot with all volumes is provided in Fig. S1, to show the huge difference between groups, which can bias all the results.

A — *Fractional Anisotropy*

	Pathway	Group	Age	Time Since Surgery	Age * Time Since Surgery
Early Visual	*Optic Tract*	0.042	0.054	0.021	**0.009**
	Optic Radiation	0.024	**0.002**	0.092	0.050
Late Visual	*Callosum Forcepts Major*	0.160	**0.009**	0.096	0.067
	Inferior Fronto-Occipital Fasciculos	0.734	**0.000**	**0.012**	0.021
	Inferior Longitudinal Fasciculus	0.840	**0.000**	**0.007**	**0.003**
	Superior Longitudinal Fasciculus	0.861	**0.000**	**0.010**	**0.006**
Motor	*CorticoSpinal Tract*	**0.000**	0.218	0.346	0.337
Other	*Cingulum Cingulate*	0.568	**0.002**	0.224	0.186
	Callosum Forcepts Minor	**0.000**	0.142	0.026	0.103
	Uncinate Fasciculus	0.022	0.036	0.033	0.055

B — *Fractional Anisotropy*

	Pathway	Group	Age	Time Since Surgery	Age * Time Since Surgery
Early Visual	*Optic Tract*	**0.000**	**0.025**	**0.026**	**0.010**
	Optic Radiation	**0.000**	**0.002**	0.088	0.042
Late Visual	*Callosum Forcepts Major*	**0.000**	**0.003**	0.109	0.066
	Inferior Fronto-Occipital Fasciculos	**0.000**	**0.000**	**0.013**	**0.021**
	Inferior Longitudinal Fasciculus	**0.000**	**0.000**	**0.008**	**0.003**
	Superior Longitudinal Fasciculus	**0.000**	**0.000**	**0.011**	**0.005**
Motor	*CorticoSpinal Tract*	**0.007**	0.063	0.423	0.353
Other	*Cingulum Cingulate*	**0.001**	**0.001**	0.221	0.171
	Callosum Forcepts Minor	0.265	0.062	0.031	0.101
	Uncinate Fasciculus	0.060	0.061	0.053	0.082

Table S3. Summary of fractional anisotropy changes in early-, late- and non-visual pathways. P-values for main effects of group, age, time since surgery (log10), and age * time since surgery (log10) interaction for ten visual and non-visual pathways when considering a reduced number of volumes in controls (A) or all recorded volumes (B). P-values smaller than 0.05 are colored light blue while bold values indicate significant effects after false-discovery rate (FDR) correction at $\alpha = 0.05$.

A

Mean Diffusivity

	Pathway	Group	Age	Time Since Surgery	Age * Time Since Surgery
Early Visual	*Optic Tract*	**0.000**	0.037	0.049	0.111
	Optic Radiation	**0.000**	0.030	0.693	0.832
Late Visual	*Callosum Forcepts Major*	**0.000**	**0.000**	**0.000**	**0.001**
	Inferior Fronto-Occipital Fasciculos	**0.000**	0.101	0.709	0.422
	Inferior Longitudinal Fasciculus	**0.000**	**0.006**	0.943	0.803
	Superior Longitudinal Fasciculus	**0.000**	**0.000**	0.117	0.310
Motor	*CorticoSpinal Tract*	**0.000**	**0.000**	0.221	0.248
Other	*Cingulum Cingulate*	**0.000**	**0.005**	0.894	0.596
	Callosum Forcepts Minor	**0.000**	**0.002**	**0.002**	0.040
	Uncinate Fasciculus	**0.000**	**0.019**	0.371	0.828

B

Mean Diffusivity

	Pathway	Group	Age	Time Since Surgery	Age * Time Since Surgery
Early Visual	*Optic Tract*	**0.000**	**0.001**	**0.010**	**0.020**
	Optic Radiation	**0.000**	**0.004**	0.193	0.370
Late Visual	*Callosum Forcepts Major*	**0.000**	**0.000**	**0.000**	**0.000**
	Inferior Fronto-Occipital Fasciculos	**0.000**	**0.029**	0.864	0.538
	Inferior Longitudinal Fasciculus	**0.000**	**0.003**	0.703	0.985
	Superior Longitudinal Fasciculus	**0.000**	**0.000**	0.053	0.207
Motor	*CorticoSpinal Tract*	**0.000**	**0.000**	0.172	0.187
Other	*Cingulum Cingulate*	**0.000**	**0.006**	0.918	0.545
	Callosum Forcepts Minor	**0.000**	**0.001**	**0.001**	**0.026**
	Uncinate Fasciculus	**0.000**	**0.004**	0.234	0.659

Table S4. Summary of mean diffusivity changes in early-, late- and non-visual pathways. P-values for main effects of group, age, time since surgery (log10), and age * time since surgery (log10) interaction for ten visual and non-visual pathways when considering a reduced number of volumes in controls (A) or all recorded volumes (B). P-values smaller than 0.05 are colored light blue while bold values indicate significant effects after false-discovery rate (FDR) correction at $\alpha = 0.05$.

Patients	Gender	Surgery Age	Diagnosis	# of Scans	Pre-surgery Acuity	Last post-surgery acuity	Time range post-surgery (log10)
P01	F	7	BCC w/ Nystagmus	1	2.3	1.9	0.48
P02	M	7	Membranous BCC	6	1.30	0.8	0.30-2.65
P03	M	9	BCC w/ Nystagmus	4	1.9	1.60	0-2.64
P04	M	10	BCC	1	2.3	1.91	3.39
P05	M	11	BCC	4	1.8	0.80	1.39-2.99
P06	F	11	Membranous BCC	2	1.93	1.30	2.93-3.08
P07	M	12	Post Polar BCC w/ Nystagmus	1	2.09	1.42	3.42
P08	M	13	Post Polar Cataract	1	2.09	1.33	3.31
P09	F	9	BCC	2	2.7	1.20	3-3.18
P10	F	13	BCC w/ Nystagmus	3	No pre-surgery acuity	2.3	2.53-3.06
P11	M	15	Membranous BCC	3	1.30	0.89	0.30-2.65
P12	M	11	Total BCC	2	2.7	1.10	3.13-3.41
P13	M	15	Total BCC w/ Nystagmus	1	2.3	1.20	3.41
P14	M	16	BCC	3	2.3	1.9	0-1.56
P15	M	17	BCC w/ Nystagmus	2	2.7	1	3.12-3.41
P16	M	16	CC	5	1.91	1.45	0-2.58
P17	M	15	CC w/ Nystagmus	4	1.9	1.63	1.20-2.51
P18	M	18	CC + Keratoglobus, corneal opacity w/ nystagmus	1	No pre-surgery acuity	No post-surgery acuity	0
P19	F	8	Pseduphakia + Psedophakia_PCO	1	1.37	1.37	0
P20	F	11	Microcornea with CC	4	1.5	1.37	0.78-2.49
P21	M	10	CC	1	1.8	1.41	1.74
P22	M	21	Microcornea, CC w/ Nystagmus (BE)	5	1.65	1.34	0-2.51
P23	M	13	CC	2	No pre-surgery acuity	1.37	1.11-1.46

Table S5. Demographic and ocular characteristics of cataract patients. Characteristics of cataract patients including gender, age at the time of cataract surgery, diagnosis (where "BCC" refers to bilateral congenital cataracts, "Post. Polar" abbreviates Posterior Polar and "CC" refers to congenital cataracts), the number of longitudinal scans acquired for each patient, the pre-surgery acuity, the last post-surgery acuity and time range post-surgery on a logarithmic scale (log10). Patients highlighted in red are the ones excluded from the analysis.

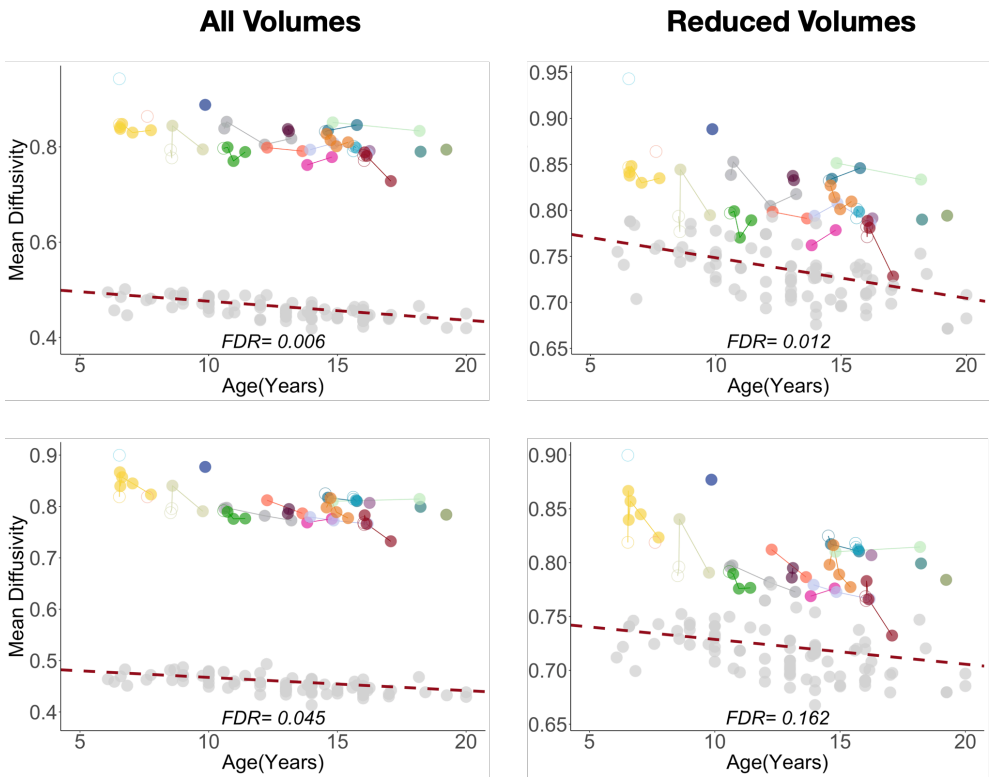

Fig. S1. Maturational changes in late-visual pathways. Example of mean diffusivity values extracted from controls and patients when using all volumes (left) or a reduced number of volumes (right), as a function of age at measurement. The plots show two late-visual tracts: Inferior Longitudinal Fasciculus (upper row) which results are significant for both all and reduced volumes and Inferior Fronto-Occipital Fasciculus (lower row) which results are significant only when including all volumes. For an exhaustive explanation of the figure, see Figs.3/4/5 in the manuscript.

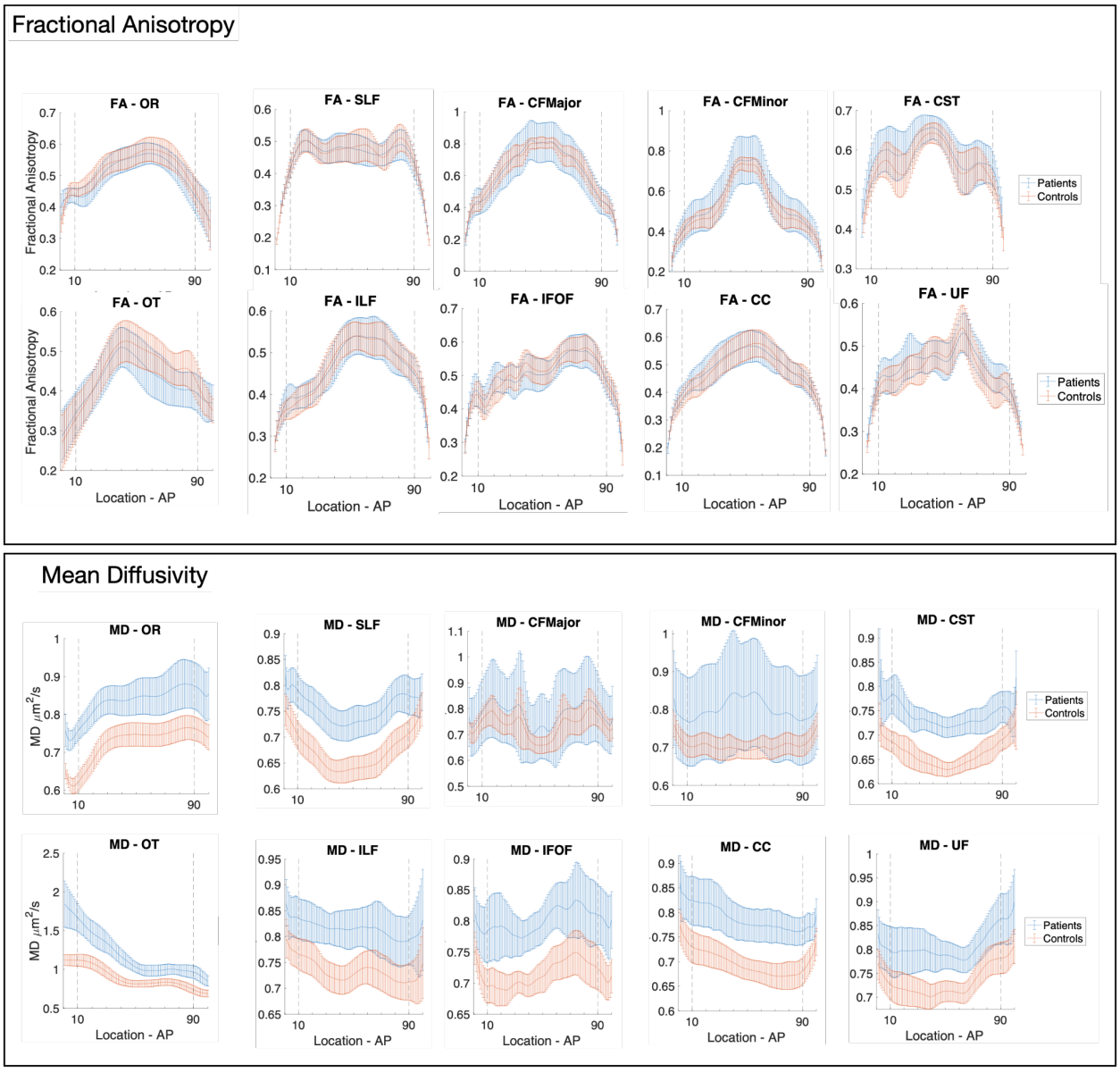

Fig. S2. Tract profiles of FA and MD. Tract mean profiles of FA and MD for patients (blue) and controls (red) along each tract following the anterior-posterior direction. Error bars indicate the standard deviation of FA or MD values of patients and controls along each tract. The range from 10 to 90 indicates the range within which the statistical analysis was performed. In this case values of controls are taken from the reduced number of volumes having a b-value < 1500.

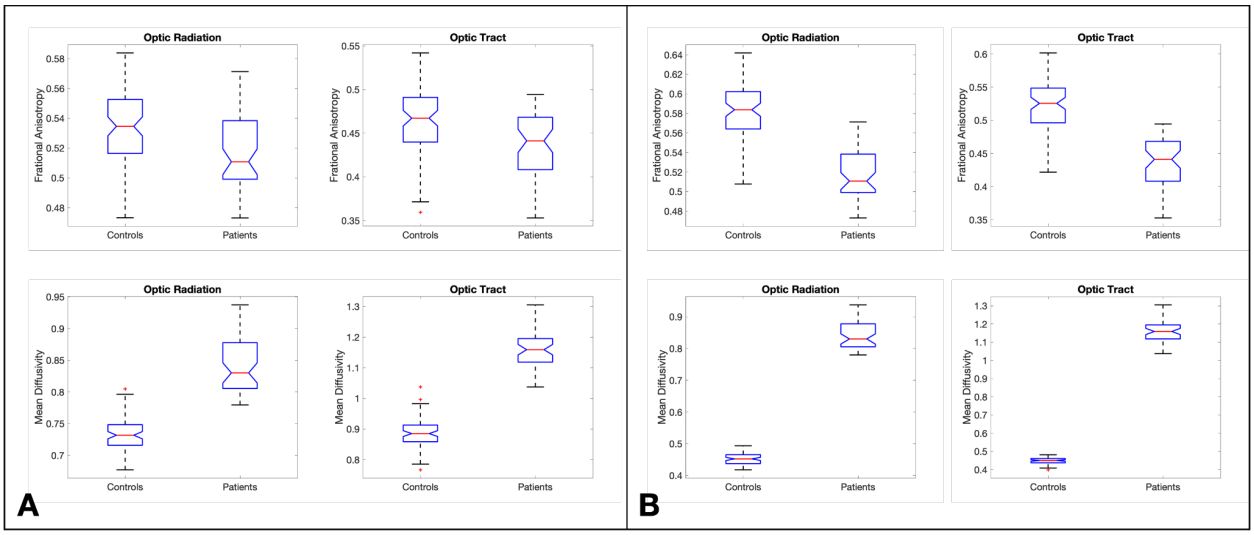

Fig S3. Fixed-effect of group in early-visual pathways. Notch Boxplot showing FA (upper row) and MD values (lower row) of controls and patients when including a reduced number of volumes (A) or all volumes (B) of controls. The red line within the notch represents the median; the upper and lower limits of the boxplot represent the 75th and 25th percentile respectively; the limits of the dashed line represent maximum and minimum values in the sample data.

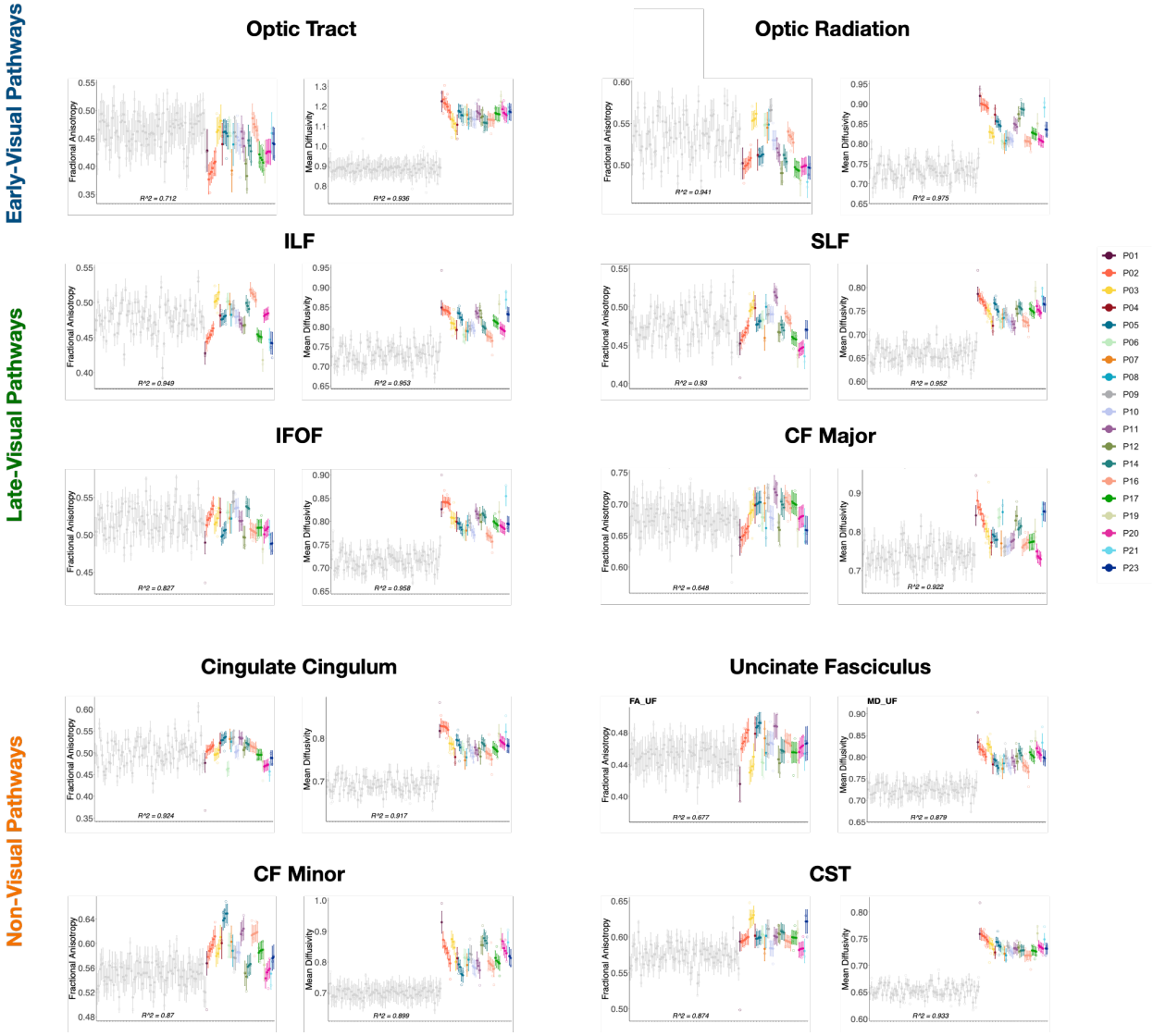

Fig. S4. **Predicted and observed values for each subject, structural measure and session for early-, late- and non-visual pathways.** Closed dots indicate the predicted values with their Confidence Interval; closed diamonds indicate the observed measure for each subject and session. Different colors indicate different patients (see legend) while all controls are color-coded in light gray. Points with the same color indicate different sessions of the same patient represented in ascending order. On the y-axes we indicate the values of fractional anisotropy or mean diffusivity. OT: optic tract; OR: optic radiation; ILF: inferior longitudinal fasciculus; SLF: superior longitudinal fasciculus; IFOF: inferior fronto-occipital fasciculus; CFMajor: posterior callosum forceps; CFMinor: anterior callosum forceps; CST: cortico-spinal tract.

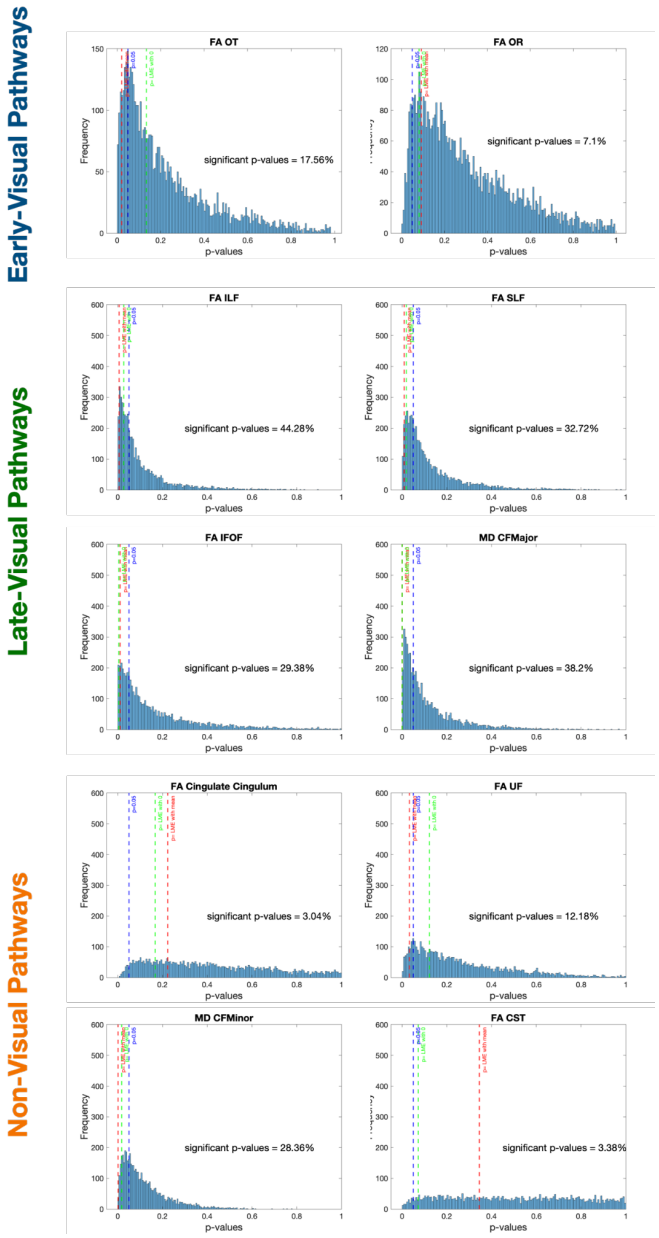

Fig. S5. Distribution of p-values of time since surgery, extracted from the 5000 iterations of the LME model for early-, late- and non-visual pathways. The blue dashed line represents the threshold of 0.05; the red dashed line represents the uncorrected p-value extracted from the LME assigning the mean value of patients to the time since surgery of controls; the green dashed line represents the uncorrected p-value extracted from the LME assigning 0 to the time since surgery of controls. The text in each plot indicates the percentage of significant p-values extracted from the 5000 iterations of the LME. The distributions skewed toward 0 indicate a higher number of low p-values, while more homogeneous distributions indicate a higher probability of extracting non-significant results. Significant results are described in the main text and they concern all the late-visual pathways and the anterior callosum forceps.

OT: optic tract; OR: optic radiation; ILF: inferior longitudinal fasciculus; SLF: superior longitudinal fasciculus; IFOF: inferior fronto-occipital fasciculus; CFMajor: posterior callosum forceps; UF: uncinate fasciculus; CFMinor: anterior callosum forceps; CST: cortico-spinal tract.

References

1. B. Allen, M. A. Schmitt, B. J. Kushner, B. Rokers, Retinothalamic White Matter Abnormalities in Amblyopia. *Invest. Ophthalmol. Vis. Sci.* **59**, 921–929 (2018).
2. K. G. Schilling, *et al.*, Synthesized b0 for diffusion distortion correction (Synb0-DisCo). *Magn. Reson. Imaging* **64**, 62–70 (2019).
3. K. G. Schilling, *et al.*, Distortion correction of diffusion weighted MRI without reverse phase-encoding scans or field-maps. *PLoS One* **15**, e0236418 (2020).
4. S. M. Smith, *et al.*, Advances in functional and structural MR image analysis and implementation as FSL. *Neuroimage* **23 Suppl 1**, S208–19 (2004).
5. J. L. R. Andersson, S. Skare, J. Ashburner, How to correct susceptibility distortions in spin-echo echo-planar images: application to diffusion tensor imaging. *Neuroimage* **20**, 870–888 (2003).
6. P. J. Basser, J. Mattiello, D. LeBihan, Estimation of the effective self-diffusion tensor from the NMR spin echo. *J. Magn. Reson. B* **103**, 247–254 (1994).
7. M. F. Glasser, *et al.*, The minimal preprocessing pipelines for the Human Connectome Project. *Neuroimage* **80**, 105–124 (2013).
8. B. Fischl, FreeSurfer. *Neuroimage* **62**, 774–781 (2012).
9. J. E. Iglesias, *et al.*, A probabilistic atlas of the human thalamic nuclei combining ex vivo MRI and histology. *Neuroimage* **183**, 314–326 (2018).
10. P. J. Basser, D. K. Jones, Diffusion-tensor MRI: theory, experimental design and data analysis - a technical review. *NMR Biomed.* **15**, 456–467 (2002).
11. T. E. J. Behrens, *et al.*, Characterization and propagation of uncertainty in diffusion-weighted MR imaging. *Magn. Reson. Med.* **50**, 1077–1088 (2003).
12. F. Calamante, J.-D. Tournier, G. D. Jackson, A. Connelly, Track-density imaging (TDI): super-resolution white matter imaging using whole-brain track-density mapping. *Neuroimage* **53**, 1233–1243 (2010).
13. T. E. Conturo, *et al.*, Tracking neuronal fiber pathways in the living human brain. *Proc. Natl. Acad. Sci. U. S. A.* **96**, 10422–10427 (1999).
14. S. Mori, P. C. M. van Zijl, Fiber tracking: principles and strategies - a technical review. *NMR Biomed.* **15**, 468–480 (2002).
15. G. J. M. Parker, H. A. Haroon, C. A. M. Wheeler-Kingshott, A framework for a streamline-based probabilistic index of connectivity (PICo) using a structural interpretation of MRI diffusion measurements. *J. Magn. Reson. Imaging* **18**, 242–254 (2003).
16. J.-D. Tournier, F. Calamante, A. Connelly, Robust determination of the fibre orientation distribution in diffusion MRI: non-negativity constrained super-resolved spherical deconvolution. *Neuroimage* **35**, 1459–1472 (2007).
17. J.-D. Tournier, F. Calamante, D. G. Gadian, A. Connelly, Direct estimation of the fiber orientation density function from diffusion-weighted MRI data using spherical deconvolution. *Neuroimage* **23**, 1176–1185 (2004).
18. J.-D. Tournier, F. Calamante, A. Connelly, MRtrix: Diffusion tractography in crossing fiber regions. *Int. J. Imaging Syst. Technol.* **22**, 53–66 (2012).
19. J.-D. Tournier, *et al.*, MRtrix3: A fast, flexible and open software framework for medical image

processing and visualisation. *Neuroimage* **202**, 116137 (2019).
20. T. Dhollander, R. Mito, D. Raffelt, A. Connelly, Improved white matter response function estimation for 3-tissue constrained spherical deconvolution in *Proc. Intl. Soc. Mag. Reson. Med*, (2019).
21. B. Jeurissen, J.-D. Tournier, T. Dhollander, A. Connelly, J. Sijbers, Multi-tissue constrained spherical deconvolution for improved analysis of multi-shell diffusion MRI data. *Neuroimage* **103**, 411–426 (2014).
22. J. D. Tournier, F. Calamante, A. Connelly, Others, Improved probabilistic streamlines tractography by 2nd order integration over fibre orientation distributions in *Proceedings of the International Society for Magnetic Resonance in Medicine*, (John Wiley & Sons, Inc. New Jersey, USA, 2010).
23. J. D. Yeatman, R. F. Dougherty, N. J. Myall, B. A. Wandell, H. M. Feldman, Tract profiles of white matter properties: automating fiber-tract quantification. *PLoS One* **7**, e49790 (2012).
24. J. D. Yeatman, B. A. Wandell, A. A. Mezer, Lifespan maturation and degeneration of human brain white matter. *Nat. Commun.* **5**, 4932 (2014).
25. J. D. Yeatman, *et al.*, The vertical occipital fasciculus: a century of controversy resolved by in vivo measurements. *Proc. Natl. Acad. Sci. U. S. A.* **111**, E5214–23 (2014).
26. A. L. Alexander, J. E. Lee, M. Lazar, A. S. Field, Diffusion tensor imaging of the brain. *Neurotherapeutics* **4**, 316–329 (2007).
27. N. Barnea-Goraly, *et al.*, White matter development during childhood and adolescence: a cross-sectional diffusion tensor imaging study. *Cereb. Cortex* **15**, 1848–1854 (2005).
28. C. Lebel, *et al.*, Diffusion tensor imaging of white matter tract evolution over the lifespan. *Neuroimage* **60**, 340–352 (2012).
29. D. Qiu, L.-H. Tan, K. Zhou, P.-L. Khong, Diffusion tensor imaging of normal white matter maturation from late childhood to young adulthood: voxel-wise evaluation of mean diffusivity, fractional anisotropy, radial and axial diffusivities, and correlation with reading development. *Neuroimage* **41**, 223–232 (2008).
30. V. J. Schmithorst, M. Wilke, B. J. Dardzinski, S. K. Holland, Correlation of white matter diffusivity and anisotropy with age during childhood and adolescence: a cross-sectional diffusion-tensor MR imaging study. *Radiology* **222**, 212–218 (2002).
31. M. Malania, J. Konrad, H. Jägle, J. S. Werner, M. W. Greenlee, Compromised Integrity of Central Visual Pathways in Patients With Macular Degeneration. *Invest. Ophthalmol. Vis. Sci.* **58**, 2939–2947 (2017).
32. Y. Benjamini, Y. Hochberg, Controlling the false discovery rate: A practical and powerful approach to multiple testing. *J. R. Stat. Soc.* **57**, 289–300 (1995).
33. T. D. Wager, M. L. Davidson, B. L. Hughes, M. A. Lindquist, K. N. Ochsner, Prefrontal-subcortical pathways mediating successful emotion regulation. *Neuron* **59**, 1037–1050 (2008).